Diffuse reflection spectroscopy at the fingertip: design and performance of a compact side-firing probe for tissue discrimination during colorectal cancer surgery

FREIJA GELDOF,[1,*] MARK WITTEVEEN,[1] HENRICUS J. C. M. STERENBORG,[1,2] THEO J. M. RUERS,[1,3] AND BEHDAD DASHTBOZORG[1] (ORCID)

[1]*Department of Surgery, Netherlands Cancer Institute, Amsterdam, The Netherlands*
[2]*Department of Biomedical Engineering and Physics, Amsterdam University Medical Center, Amsterdam, The Netherlands*
[3]*Faculty of Science and Technology, University of Twente, Enschede, The Netherlands*
[*]*f.geldof@nki.nl*

Abstract: Optical technologies are widely used for tissue sensing purposes. However, maneuvering conventional probe designs with flat-tipped fibers in narrow spaces can be challenging, for instance during pelvic colorectal cancer surgery. In this study, a compact side-firing fiber probe was developed for tissue discrimination during colorectal cancer surgery using diffuse reflectance spectroscopy. The optical behavior was compared to flat-tipped fibers using both Monte Carlo simulations and experimental phantom measurements. The tissue classification performance was examined using freshly excised colorectal cancer specimens. Using the developed probe and classification algorithm, an accuracy of 0.92 was achieved for discriminating tumor tissue from healthy tissue.

1. Introduction

Colorectal cancer is currently the third most common cancer type, with more than 1.9 million new patients worldwide in 2020 [1]. The preferred treatment for colorectal cancer is surgery combined with (neo)adjuvant chemo- and/or radiotherapy. The aim of colorectal surgery is to remove the entire tumor, while sparing the surrounding healthy structures as much as possible. The surgical resection margin (SRM), which is defined as the shortest distance between the resection surface and the tumor, is an important prognostic factor for patient outcome. A radical tumor resection, in which a sufficient margin of healthy tissue is removed both circumferentially and distally to the tumor, reduces the risk of local tumor recurrence and increases the survival rate [2–4]. However, identifying the tumor and consequently the optimal resection margin during surgery can be challenging, which can lead to incomplete tumor removal. Incomplete tumor resection rates of up to 30 percent have been reported for locally advanced colorectal cancer surgeries [2–6]. On the other hand, too extensive resection may damage vital surrounding tissue such as blood vessels, nerves, and ureters, leading to serious complications or may lead to permanent bowel incontinence as well as bladder and sexual dysfunction [7–11]. Poor functional outcome, especially fecal incontinence, has a major effect on a patient's overall well-being and quality of life.

The current gold standard for determining the surgical resection margin status is based on histopathological examination which takes approximately one week. In addition, surgeons can send a small tissue sample for frozen section analysis during surgery, which still takes about 30 minutes. Real-time intra-operative tissue discrimination, however, cannot be provided.

Consequently the absence of an intraoperative anatomic assessment tool comes at the cost of surgical complications and impairment of patients' quality of life as well as incomplete tumor resection and the necessity of additional treatments.

A real-time tissue discrimination technique could provide surgeons with immediate intra-operative guidance on optimal resection margins. Within this context, diffuse reflectance spectroscopy (DRS) has been widely examined for tissue sensing and discrimination. DRS is a fast and non-invasive optical technology that sends broadband light into the tissue using a source fiber. The reflected light is detected with a second detection fiber, after undergoing several scattering and absorption events in the tissue. The reflectance spectrum contains spectral signatures and information about the optical properties of the measured tissue. DRS has already been successfully used for colorectal cancer detection, such as for classifying polyps during colonoscopy [12,13] and distinguishing tumor tissue from healthy tissue during ex-vivo measurements on freshly excised colorectal cancer specimens [14–17] and in-vivo measurements during open colorectal cancer surgery [18].

The optical probes that were used in these previous studies consisted of widely used flat-tipped optical fibers, in which the light exits the fiber from the front as shown in Fig. 1. For proper optical contact, these fibers, and therefore also the probe, must be placed perpendicular to the tissue surface of interest. As a result, it can be difficult to reach certain locations with an optical probe, such as narrow spaces low in the abdomen during rectal cancer surgery with limited space to move. In addition, the fact that surgeons have to use a new and additional tool for tissue discrimination can make it challenging to retrieve the exact locations measured. Since surgeons normally often palpate areas of questionable tumor involvement during surgery, it would be a great advantage if they could perform tissue discrimination measurements directly underneath their fingertips. The improved ergonomics of a side-firing fiber tool could contribute to a more frequent use and an improved feasibility of diffuse reflectance spectroscopy in clinical practice. In order to position the optical fibers on a compact probe or at the tip of the surgeon's finger, and to be able to maneuver in narrow spaces, the use of side-firing optical fibers might be a solution.
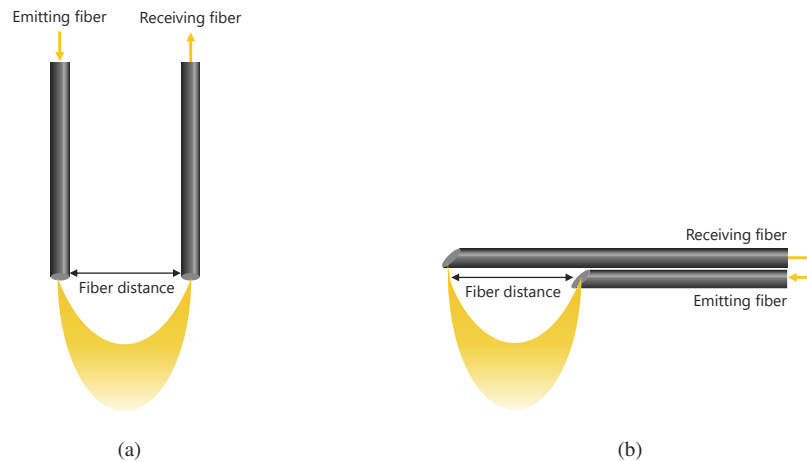

(a)   (b)

Fig. 1. Optical probe configurations using flat-tipped fibers (a) and side-firing fibers (b). Flat-tipped optical fibers emit light straight to the front and must therefore be placed perpendicular to the tissue surface. The tips of side-firing optical fibers are polished under an angle that causes total internal reflection, which results in light emission through the side of the fiber and means that they can be placed parallel to the tissue surface.

One way of producing side-firing optical fibers is to give it an obliquely polished tip, at an angle that causes total internal reflection. As a result, the light is emitted under an angle through

the side of the optical fiber instead of straight to the front, as shown in Fig. 1(b) [19–21]. By polishing the detection fiber under an angle as well, the diffusely reflected light can still be collected and analyzed. Using side-firing fibers could enable a more compact tissue probe which can be used during surgery when there is limited space or areas that are hard to reach.

A number of studies can be found in which side-firing fibers have already been used for various optical techniques in different applications. One of these applications is the incorporation of side-firing fibers in a core-biopsy needle that is used for breast cancer research [22–24]. Lubawy *et al.* developed a probe with two source fibers and one detector fiber, that can be inserted into the biopsy needle. By performing near-infrared (NIR) photon migration spectroscopy measurements on a phantom with heterogeneities, absorption coefficients could be predicted with an error of up to 30% compared to theoretical values [22]. Using the same probe, Yu *et al.* performed preliminary NIR diffuse optical spectroscopy measurements on breast tissue from five women undergoing core-biopsy [23]. Pearson's correlation coefficients were calculated between extracted tissue optical properties and histologically derived tissue compositions. Subsequently, Zhu *et al.* used this probe to assess the feasibility of fluorescence spectroscopy (FS) measurements during breast biopsy procedures [24]. Using a principal component analysis, the biopsy samples were classified as malignant or non-malignant with a sensitivity and specificity of 81% in 51 patients. This is the only study with a side-firing fiber probe that has been performed to classify certain tissue types in human tissue. However, where this study is using FS, we are planning to use DRS.

Other studies have been performed on the use of a side-firing fiber probe for tissue oxygenation measurements over time [25–27]. Yu *et al.* used an upgraded version of the side-firing fiber probe described above to quantify changes in tumor oxygenation and hemoglobin concentration in rats using a frequency-domain photon migration system with six laser wavelengths between 654 and 905 nm [25]. Baran *et al.* created a probe with six side-firing fibers arranged in different radial directions to monitor interstitial photodynamic therapy (PDT) treatment using white light spectroscopy [26]. Absorption coefficients, scattering coefficients and hemoglobin oxygen saturations of tissue-simulating phantoms could be recovered with mean errors of 9%, 19%, and 12% respectively. Also, Ong *et al.* used side-firing fibers for PDT monitoring [27]. Tissue oxygenation levels were measured over time using diffuse correlation spectroscopy, for both mice and seven patients.

Finally, there are studies in which an ultrasound catheter is combined with a side-firing photo-acoustic imaging system [28–30]. Karpiouk *et al.* added a side-firing fiber onto an intravascular ultrasound catheter, in which the polishing angle of the optical fiber was chosen in such a way that the photoacoustic laser beam had the best alignment with the ultrasound imaging beam [28]. After that, Basij *et al.* developed a comparable system for cervical cancer imaging, but this time six side-firing fibers have been used for the photoacoustic laser beam to illuminate the sample [29,30]. The ability of these combined probes to acquire and co-register the volumetric US and photoacoustic images and to detect certain inclusions in the volume have been evaluated in (porcine) phantoms.

In summary, several studies can be found in which side-firing fibers already have been used. However, to the best of our knowledge no research has been done yet on the use of side-firing fibers for broadband diffuse reflectance spectroscopy (400-1600nm), and in particular tissue type classification and tumor distinction in colorectal tissue. The aim of the current study is to assess the feasibility of using side-firing fibers instead of flat-tipped fibers for surgical margin assessment using DRS during colorectal cancer surgery. To this end, Monte-Carlo simulations and experimental measurements in a two-layered phantom are performed to compare the measurement depth and efficiency of side-firing fibers with flat-tipped fibers. By investigating any differences between the two fiber configurations, this can be taken into account during use in practice. In addition, we will assess the ability of side-firing fibers to predict layer thicknesses.

Finally, the feasibility of side-firing DRS for tissue classification is examined in an ex-vivo study using freshly excised colorectal cancer specimens.

The remainder of this paper is organized as follows: Section 2. describes the developed optical probe using side-firing fibers and the diffuse reflectance spectroscopy system. Sections 3. and 4. describe the data acquisition and data analysis methods that were used for the assessment of measurement depth and development of a tissue classification algorithm, respectively. The results are presented in Section 5, which is followed by the discussion and conclusion in Sections 6 and 7.

2. Materials

2.1. Side-firing optical fiber probe

Two silica-silica fibers with a core diameter of 365 μm and an NA of 0.22 were used; one as source fiber and one as detector fiber. The tips of both fibers were polished at an angle of 45° to ensure the light exits the fiber perpendicular to the fiber orientation. Using biocompatible glue the fibers were fixated in a quartz cap, with a diameter of 2.3 mm and length of 12 mm, to create an air–glass interface (see Fig. 2). Inside the cap, the polished tips of the fibers were oriented in the same orientation with a source-to-detector fiber distance (SDD) of 2.7 mm.
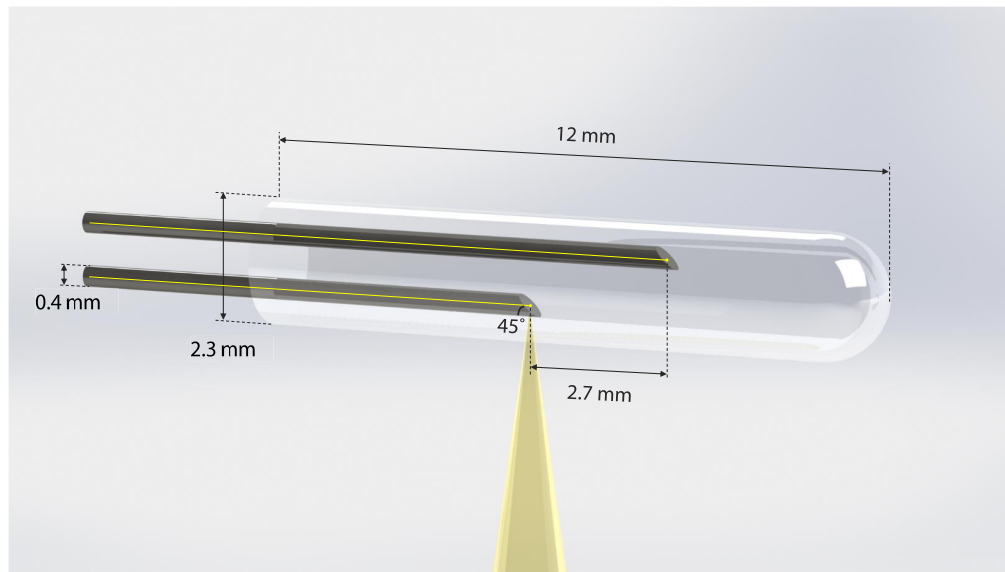

Fig. 2. Schematic representation of two side-firing optical fibers (one source and one detector fiber) fixated in a quartz cap, with an equal orientation of polished fiber tips and a fiber tip distance of 2.7 mm. Both optical fibers are polished at an angle of 45°.

To ensure that the light will reflect through the side of the fiber, total internal reflection is needed. Total internal reflection can be achieved using a critical angle $\theta_{critical}$ (Eq. (1)) [28,29]:

$$\theta_{critical} = \arcsin\left(\frac{n_{medium}}{n_{core}}\right) \tag{1}$$

where n_{medium} and n_{core} represent the refractive indices of the medium outside the fiber and the fiber core, respectively. The angular range ($\theta_{Refl1} < \theta < \theta_{Refl2}$) under which the light beam will be

reflected from the fiber can be calculated using Eqs. (2) and (3) [28,29]:

$$\theta_{Refl1} = 2 * \beta - \left(90° - \arcsin\left(\frac{n_{cladding}}{n_{core}}\right)\right) \tag{2}$$

$$\theta_{Refl2} = 90° - \theta_{critical} + \beta \tag{3}$$

where β represents the polishing angle of the fiber tip and $n_{cladding}$ the refractive index of the fiber cladding.

For the side-firing fiber probe used in this study, with a polishing angle of 45°and air around the fiber due to the use of the quartz cap, this means that the light beam is emitted with an angular range of 81°to 92°relative to the horizontal axis (fiber orientation).

2.2. Finger tip probe

The side-firing optical fiber pair described above is incorporated in a 3D printed prototype of a finger tip probe model as demonstrated in Fig. 3. This prototype can be worn on the tip of the index finger, which allows surgeons to do optical measurements directly at the tip of their fingers without the need for additional large instruments. The finger tip prototype was printed using gray photopolymer prototyping resin (Formlabs, Somerville, Massachusetts, United States) and a Form 3 3D printer (Formlabs, Somerville, Massachusetts, United States). The side-firing fiber bundle was fixated with glue on the prototype in such a way that the light beam exits the probe perpendicular to the finger tip. The fingerprint adapter has been designed in a way that ensures that the fibers are always parallel to and in contact with the tissue.
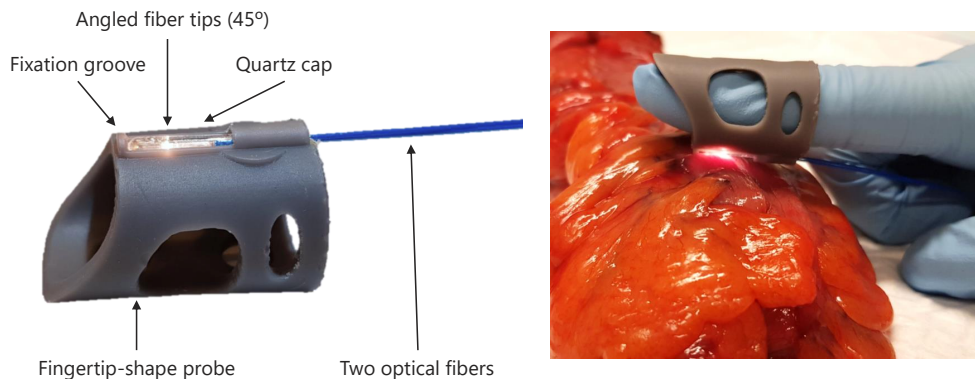

Fig. 3. Side-firing fiber probe incorporated in a 3D printed finger tip prototype (*left*), which can be worn on the index finger to perform optical measurements on colorectal tissue (*right*).

2.3. Diffuse reflectance spectroscopy system

The DRS system consisted of a halogen broadband light source (Avantes, AvaLight-HAL, 360 – 2500 nm) and two spectrometers: one for the visible wavelength range from 200 to 1160 nm (Avantes, AVASPEC-HS2048XL-EVO) and the other for the near-infrared range from 900 to 1750 nm (Avantes, AVASPECNIR256-1.7-RS). In-house developed MATLAB software was used to control these components and process the data.

All diffuse reflectance spectra were calibrated using a white reference measurement (with Spectralon; Avantes WS-2, Avantes, Apeldoorn, the Netherlands) to correct for the spectral shape of the lamp and sensitivity of the system, and a dark reference measurement (switching off the

light source) to correct for the ambient light and dark current, see Eq. (4):

$$R_{cal} = \frac{R_{meas} - R_{dark}}{R_{white} - R_{dark}} \tag{4}$$

in which R_{cal} is the calibrated measurement, R_{meas} is the uncalibrated measurement, R_{dark} is the dark reference measurement and R_{white} is the white reference measurement.

The spectra from the visible and near-infrared wavelength ranges were stitched together by the DRS software, to create one spectrum ranging from 400 – 1600 nm. The data up to 400 nm and after 1600 nm has been removed due to a low signal-to-noise ratio.

3. Measurement depth

An optical probe should measure up to a certain depth into the tissue to sense the specific region of interest, especially for tumor detection within the resection margin during surgery. In addition, any differences in the measurement depth should be taken into account before comparing and/or exchanging DRS spectra acquired with different probes. To this end, Monte-Carlo simulations and experimental measurements in a two-layered phantom are performed to compare the light behaviour and measurement depth of side-firing fibers with flat-tipped fibers. The ability of side-firing fibers for predicting layer thicknesses is investigated using the two-layered phantom as well.

3.1. Monte Carlo analysis

To investigate the illumination and collection setup of the side-firing fibers and compare the measurement depth with conventional flat-tipped fibers, a Monte Carlo simulation was performed. The simulations were performed using GPU-accelerated mesh-based Monte-Carlo software (MMC), as used by Fang, Q, & Yan, S (2019) [31]. This allows the simulation of the illumination of the side-firing fiber by the creation of a tetrahedral mesh of the fiber and homogenous generic tissue. The adjoint method was used to calculate the Jacobian of the absorption for the flat and side-firing fibers [32]. In the adjoint method, a simulation is performed twice. First the source is simulated, after which the detector is simulated as a source, and the fluence of both simulations are convoluted. The resulting Jacobian is an indication of the sensitivity of the measurement setup to absorption in the simulated volume. A simulation volume of $18 \times 20 \times 16$ mm was used. The absorption and scattering properties of the tissue were chosen to represent a generic soft tissue [$\mu_a = 0.445\ mm^{-}1$; $\mu_s = 1.89\ mm^{-}1$] [33]. For the fiber, the core and cladding were given their appropriate refractive indices. A diverging Gaussian light source was used for both the flat-tipped and side-firing fibers. The quartz-cap as seen in Fig. 2 is not included in the simulation. The resulting profiles can then be compared to gauge measurement depths for the two types of fibers.

3.2. Phantom study

A phantom study was performed to examine the light behaviour and measurement depth of an optical probe with side-firing fibers in an experimental setup, and to compare it with an optical probe with flat-tipped fibers. In addition, the ability of side-firing fibers to predict tissue layer thicknesses was evaluated as well.

3.2.1. Phantom creation

A bilayer phantom was created, in which both phantom layers consisted of water-dissolved agarose as the base material (Sigma-Aldrich, 0.84% concentration) and Intralipid as the scattering material (Intralipid-20% solution, 5% concentration). In the bottom layer, Methylene blue (Proveblue 5 mg/mL, 0.28% concentration) was added as an absorbing agent, which strongly

absorbs light around a wavelength of 664 nm. The thickness of the bottom layer thickness was equal to 20 mm, while the top layer thickness gradually increased from 0 to 5 mm. Figure 4 shows a schematic representation of the created bilayer phantom, in which the intersection points between lines represent the different measurement locations.
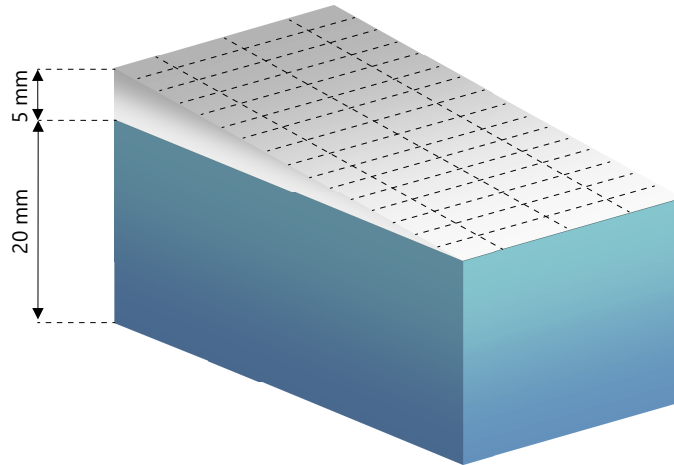

Fig. 4. Schematic representation of the bilayer phantom. The top layer thickness varies from 0 to 5 mm, which results in a variable distance from the measurement surface to the bottom layer with Methylene blue. The intersections between the dashed lines on the phantom surface represent the different measurement locations, in a grid pattern.

3.2.2. Measurement protocol

As demonstrated in Fig. 4, DRS measurements were performed on the bilayer phantom in a grid pattern, with fifteen measurements along the length of the phantom and three measurements along the width of the phantom, resulting in 45 measurement locations in total. At each location, a measurement was performed using both the side-firing fiber probe, as well as using a conventional flat-tipped fiber probe with six different fiber distances (1,2,3,4,6,8 mm). Per measurement location three DRS spectra were acquired, which were averaged afterwards. After the data acquisition, the phantom was cut at the measurement locations to obtain all the actual corresponding top layer thicknesses (ground truth) using a ruler.

3.2.3. Data analysis

To compensate for any intensity differences due to various fiber distances, different applied probe pressure, or changes in the environmental light condition, the broad-band spectra were normalized using a standard normal variate (SNV) normalization technique, in which each spectrum has its mean subtracted and is then divided by its standard deviation.

Methylene blue, which was added to the bottom layer of the phantom, strongly absorbs light around a wavelength of 664 nm. The presence of a reflection dip in this region of the DRS spectrum indicates that the bottom layer of the phantom has been measured. Therefore, the magnitude of this Methylene blue dip for different top layer thicknesses of the phantom will give an indication of the measurement depth of the side-firing fibers.

Similar to the previous work by Geldof *et al.* [34], we investigated the prediction of the top layer thickness for every measured location using side-firing fibers and a machine learning (ML) model, which could ultimately translate to surgical resection margin assessment. To examine the feasibility of using side-firing fibers for predicting layer thicknesses, a regression analysis was

performed using the DRS spectra that were acquired on the bilayer phantom using the side-firing fiber probe. The normalized intensity values from the entire range of 400 to 1600 nm were used as input features for training the regression model and the corresponding top layer thicknesses of every measurement location were used as output labels. A Gaussian Process Regression (GPR) ML model was trained using a 20-fold cross-validation approach. The average prediction error of all 20-folds was used for the overall performance assessment of the trained algorithm.

Lastly, the measurement depth of the optical probe with side-firing fibers was compared to that of the conventional flat-tipped fiber probe. The correlation coefficients between the DRS spectra acquired with the side-firing fiber probe (SDD of 2.7 mm) and the spectra acquired with the flat-tipped probe (six different SDD's) were calculated for all 45 measurement locations on the phantom.

4. Tissue classification

The ability to accurately distinguish tumor tissue from multiple types of healthy tissue is crucial for providing intra-operative margin assessment. Previous studies already explored the use of DRS with conventional flat-tipped fibers for tissue classification. In the current study, the tissue classification feasibility of the developed side-firing DRS probe is examined in an ex-vivo study using freshly excised colorectal cancer specimens and machine learning techniques. In this section, the workflow for data acquisition, correlation with histopathology ground truth results, and tissue classification will be described.

4.1. Patient inclusion

To examine the feasibility of tissue discrimination using a side-firing optical fiber probe, freshly excised colorectal specimens were used. Nine patients that were diagnosed with colorectal cancer and underwent a surgical resection in the Antoni van Leeuwenhoek hospital - Netherlands Cancer Institute were included between October 2021 and March 2022. Patients were included when they were diagnosed with a T3 or T4 stage tumor in the colon, sigmoid, or rectum, based on preoperative examinations. This study has been performed under the approval of the Hospital Ethics Review Board and all patients have given permission for the further use of their data and biological materials for scientific research.

4.2. Measurement protocol

The workflow of data acquisition is demonstrated in Fig. 5(a). Directly after resection, the colorectal specimens were collected to perform DRS measurements with the side-firing fiber probe. First, the tumor site was determined using palpation and ultrasound imaging. On the tumor site, three DRS measurements were performed on one to three lines, depending on the tumor size. Immediately after each measurement, the measured location was marked with ink to be able to track the measurement location and correlate it with the histopathological results. Per measurement line, two colors of ink were used (black and orange) to be able to determine the orientation. Next, five DRS measurements were performed randomly on both healthy muscle tissue and healthy fat tissue, indicated by the green and blue dots. Since these locations were chosen at least 1 cm outside the tumor area that was found using ultrasound imaging, and muscle and fat tissue are clearly distinguishable visually, no ink marks for histopathology correlation were placed at these locations. Nevertheless, the absence of tumor in the healthy measurement locations was confirmed based on pathology reports.

4.3. Correlation with histopathology

As demonstrated in Fig. 5(b), the colorectal specimens were brought to the pathology department after performing the measurements, where they were fixated and sliced according to the standard
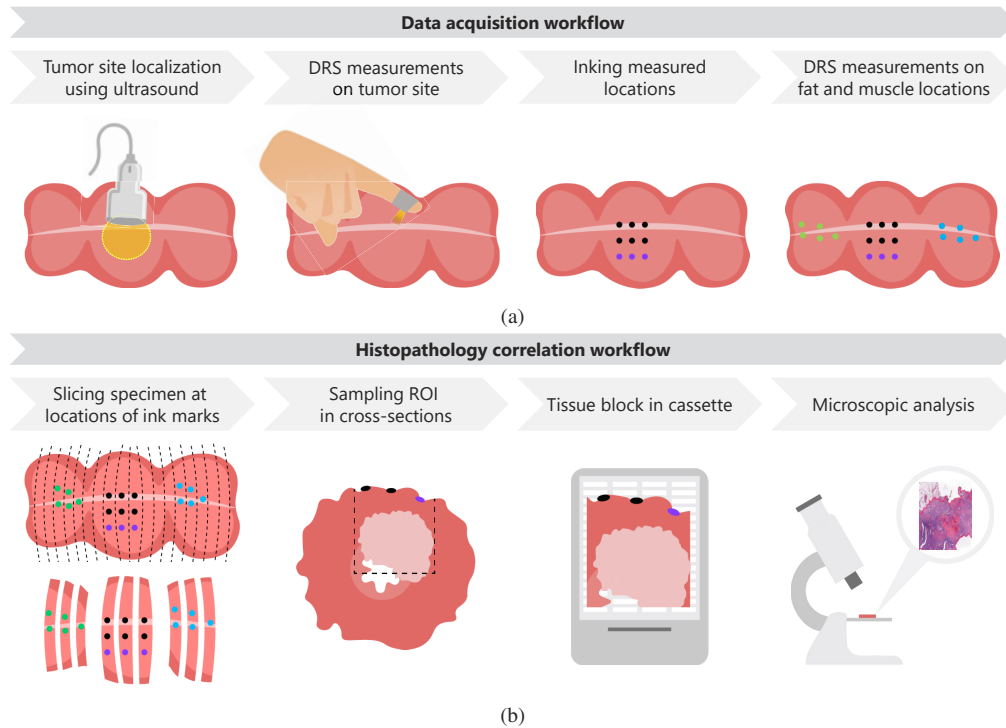
Fig. 5. (a) Data acquisition workflow: First, the tumor site is localized in the freshly excised rectal specimen using ultrasound imaging (dashed yellow circle). In the next step, three to nine DRS measurements were performed using the side-firing fiber probe in this area, depending on the specimen size. Immediately after each measurement, the measurement location was marked with ink to allow correlation with histopathological results. The green and blue dots represent five DRS measurement locations on healthy muscle and fat tissue, respectively. (b) Histopathology correlation workflow: After finishing the data acquisition, the specimen was taken to the pathology department for further processing according to standard protocols. The specimen was fixated in formalin, after which it was dissected in slices. From these slices, the areas with ink marks on the surface were sampled in cassettes. The final H&E sections were digitally scanned for microscopic analysis and were annotated by a pathologist, who delineates fat, healthy rectal muscle, and tumor areas. The black and orange ink marks, representing the exact measurement locations, can be found back in the digital tissue slices as well as on the border of H&E images. In this way, tumor presence can be confirmed for every measurement location.

protocol. Next, the slices were H&E stained, digitized and microscopically assessed by a pathologist, see Fig. 6. The ink marks that were placed during data acquisition indicate the measured locations in the digital tissue slices. The ground truth labels (tumor, muscle, fat) for every measurement were assigned based on the pathology report of the corresponding tissue sections.
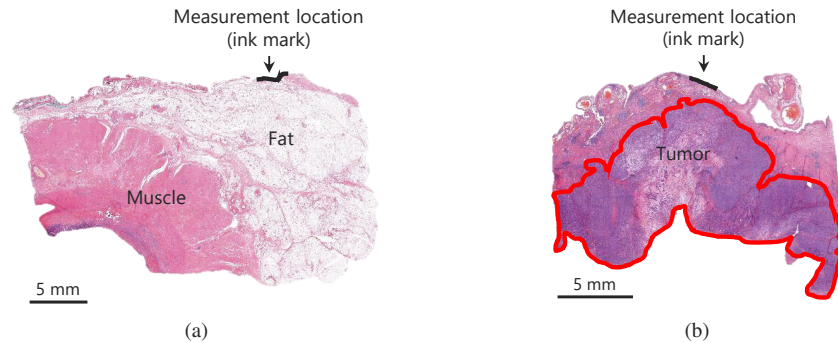

Fig. 6. Examples of H&E stained histopathology slices for a healthy fat location (a) and a tumor location (b). The black ink marks at the tissue surface indicate the measured locations. The tumor area, delineated by a pathologist, is shown in red.

4.4. Data analysis

A supervised classification model was trained to predict the tissue types of measured locations with the side-firing DRS probe. The acquired broad-band spectra (after normalization at 800nm) were used as input, while the ground truth labels based on the pathology results were used as the output labels for training the model. A support vector machine (SVM) model with a quadratic kernel was trained using 10-fold cross-validation to classify the measured tissue types. To evaluate the performance of the model, the area under the curve (AUC), accuracy, sensitivity, specificity, and Matthews Correlation Coefficient (MCC) were calculated using an average of 10 iterations.

4.4.1. Feature selection

In order to prevent overfitting due to a relatively large number of features (1201 wavelengths) compared to the number of sample points, a minimum redundancy maximum relevance (MRMR) feature selection algorithm was used to calculate the feature importance score for all wavelengths [35]. The MRMR feature selection method returns a subset of features by an iterative selection of features that are maximally relevant for the prediction task and minimally redundant with the set of already selected features. Using the results of MRMR, the 90 most important features were selected as input for training the machine learning model. The number of selected features was chosen by experiments on increasing the number of selected features, training the classification model and evaluating the performance. The iteration was stopped after no further improvement was observed. The performance using only the selected wavelengths was compared with using all wavelengths as input.

5. Results

In this section, the results of the measurement depth assessment using Monte Carlo analyses and bilayer phantom experiments (as described in Section 3) will be presented first, after which the performance of the developed tissue classification algorithm (as described in Section 4) will be evaluated.

5.1.　Measurement depth

5.1.1.　Monte Carlo analysis

The results of the Monte Carlo simulations are presented in Figs. 7 and 8. In Fig. 7, the Jacobian to the absorption is shown midway between the source and detector, for the flat-tipped fiber, the side-firing fiber, and a comparison side by side. The Jacobian for the flat-tipped fiber has a higher intensity, with higher values at deeper depths compared to the side-firing fiber with the same source-to-detector distance. This difference is best seen in the comparison figure (Fig. 7(c)), where the outer contour for the flat-tipped fiber and the side-firing fiber differ by approximately 1 mm. Figure 8 shows the side profiles for the flat-tipped fiber and the side-firing fiber. There is again a clear difference in the shape of the profile and the depth that it reaches. The side-firing fibers show lower values and reach a smaller depth compared to the flat-tipped fibers.
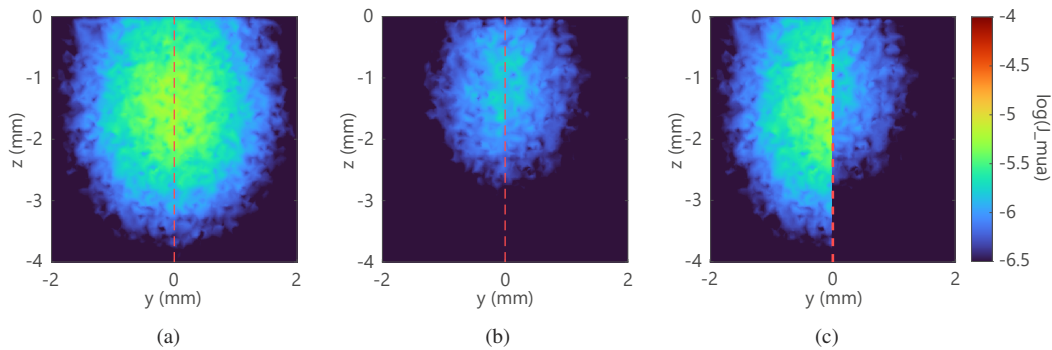

Fig. 7. The head-on Jacobian profiles for the flat-tipped fiber (a), the side-firing fiber (b), and a combination of both split through the center (c), all for a source-to-detector distance of 2.7 mm. The Jacobian for the flat-tipped fiber is higher at equal depth, with higher values at deeper depths compared to the side-firing fiber.
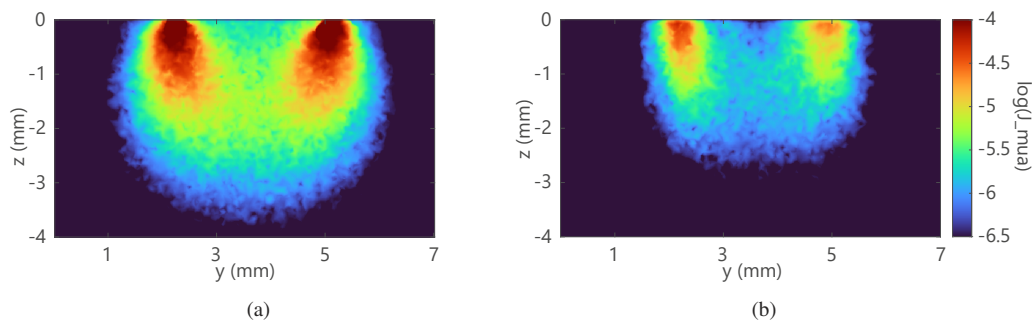

Fig. 8. The side profiles of the Jacobian for the flat-tipped fibers (a) and the side-firing fibers (b). The side-firing fibers (b) are positioned as shown in Fig. 2 and the source-to-detector distance in both figures is 2.7 mm.

A comparison of the relative signal at different depths is presented in Fig. 9. This comparison shows the cumulative signal along the z-axis through the middle of the volume normalized by the total signal, such that at the top of the tissue (z = 0 mm) the value is 100%. The cumulative signal can be used to compare the measurement depth between the two configurations without using any absolute values, as in the proposed setup the signal can be increased to compensate for the reduced signal due to the side-firing fiber configuration. The comparison shows that even

when compensating for the loss of signal with the side-firing fibers, the side-firing fibers have reduced measurement depth compared to the flat-tipped fibers.
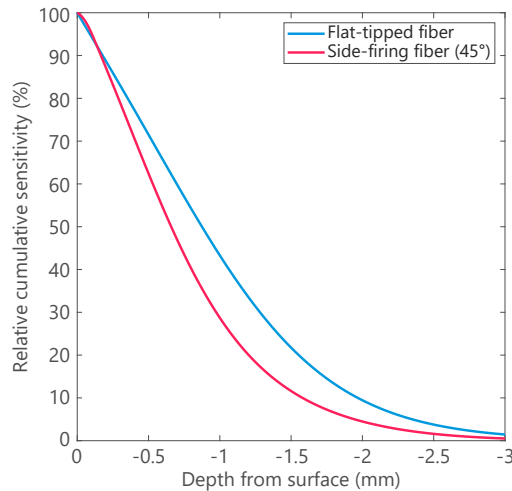

Fig. 9. The cumulative signal along the z-axis through the middle of the volume normalized by the total amount of signal. Due to the normalization of the total signal the difference in signal over depth is smaller than in Figs. 7 and 8, but a clear difference remains between the two fiber types. The side-firing fibers have reduced signal at deeper depths compared to the flat-tipped fiber, with a slight increase of signal in the first 0.135 mm.

5.1.2. Phantom study

The DRS spectra for all 45 measurement locations on the bilayer phantom, which were acquired using a side-firing fiber probe, are shown in Fig. 10(a). The color of each line represents the top layer thickness at the measured locations, which corresponds to the distance between the measurement surface and the Methylene blue layer (second layer). In all spectra, a reflectance dip is visible around 664 nm, the peak absorption wavelength of Methylene blue, which becomes less apparent as the top layer thickness of the phantom increases. A clear correlation can be seen between the top layer thickness and the size of this reflectance dip.

By training a regression model, the top layer thickness (or distance to the Methylene blue layer) could be predicted with a root mean square error (RMSE) of 0.23 mm and a mean absolute error (MAE) of 0.18 ± 0.14 mm. Figure 10(b) shows the predicted top layer thickness versus the true top layer thickness for all measurement locations. The Pearson correlation coefficient of 0.985 indicates an excellent correlation between the predicted and the true values.

The spectra that were acquired using a conventional flat-tipped fiber probe, at the same locations on the bilayer phantom as the side-firing fiber measurements, are shown in Fig. 11. These spectra show the same general characteristics as the spectra acquired using the side-firing probe (Fig. 10(a)), with again the dip in reflection intensity in the wavelength region around 664 nm due to the absorption by Methylene blue in the bottom layer. In this wavelength region, clear differences in reflection dip height can be seen between the spectra from different fiber distances. The correlation coefficients between the DRS spectra acquired with the side-firing fiber probe (SDD of 2.7 mm) and the spectra acquired with the flat-tipped probe (six different SDD's) are shown in Fig. 12 for all measurement locations on the phantom. The highest correlation coefficients were found for flat-tipped fibers with an SDD of 1 and 2 mm. These results demonstrate that the DRS spectra of our side-firing fiber probe with an SDD of 2.7 mm
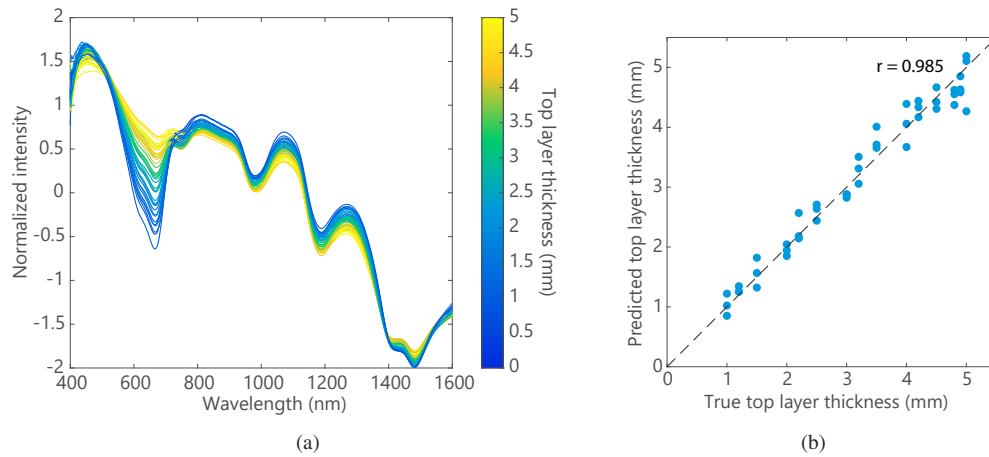
Fig. 10. (a) DRS spectra of all measurement locations on the bilayer phantom, acquired using a side-firing fiber probe with a source-detector fiber distance of 2.7 mm (after SNV). The line color indicates the top layer thickness at the measured locations, which is equal to the distance to the Methylene blue layer (recognizable by the absorption dip at 664 nm), (b) Predicted top layer thickness versus true top layer thickness for all measurement locations on the bilayer phantom.

are most comparable to spectra of a conventional flat-tip fiber probe with a smaller SDD of around 1 to 2 mm.
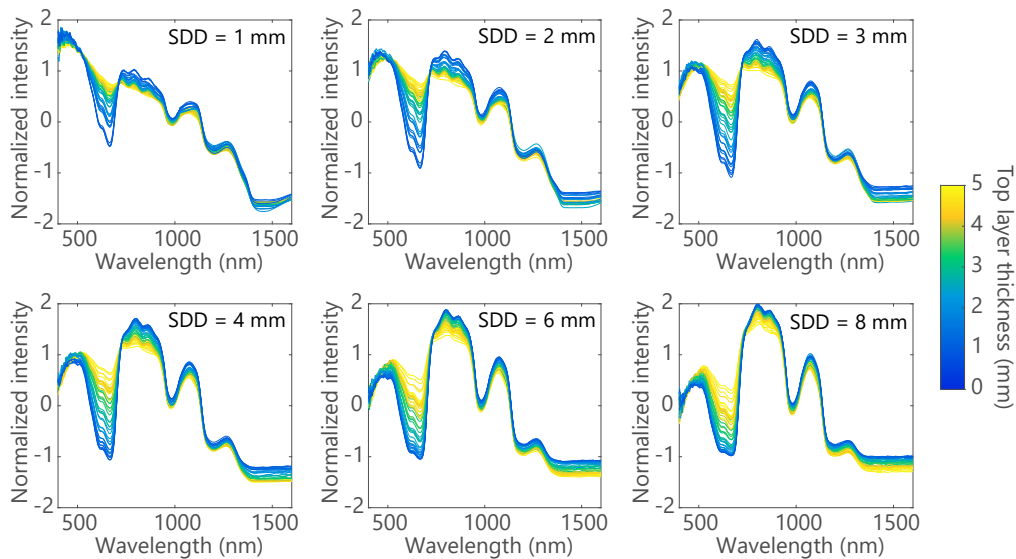

Fig. 11. DRS spectra of all measurement locations on the bilayer phantom, acquired using a conventional flat-tipped fiber probe with six different fiber distances (1, 2, 3, 4, 6, 8 mm). The line color indicates the top layer thickness at the measured locations, which is equal to the distance to the Methylene blue layer (absorption at 664 nm).
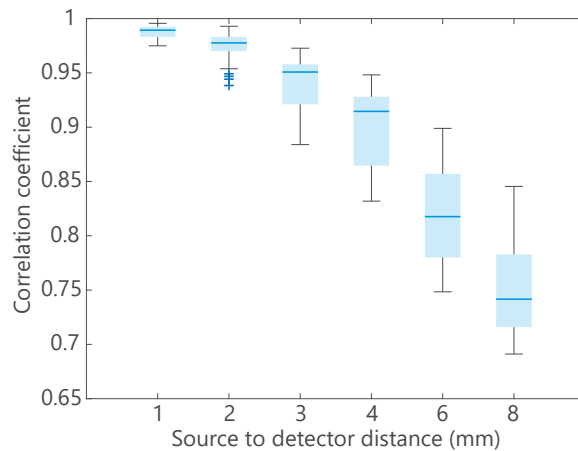
Fig. 12. Boxplots of the correlation coefficient between the DRS spectra acquired with the side-firing fiber probe (SDD of 2.7 mm) and the spectra acquired with the flat-tipped probe (six different SDD's). These are the results of a location-wise comparison for all 45 measurement locations on the phantom, with different distances to the Methylene blue layer.

5.2. Tissue classification

Nine freshly excised colorectal cancer specimens were included in this study. DRS measurements were performed on 150 locations in total; 46 fat locations, 45 muscle locations and 59 tumor locations (confirmed by histopathology). Figure 13 shows the mean DRS spectra for fat, muscle and tumor tissue, acquired using the side-firing fibers. The bottom figure shows the feature importance score per wavelength, resulting from the MRMR analysis. The 90 most important features that were selected by the MRMR analysis are highlighted by the grey lines in the top figure.

The performance of the tissue classification model is shown in Table 1, both for all features and only the most important features. Feature selection improved the classification accuracy from 0.88 to 0.92, compared to using all wavelengths. The sensitivity, specificity, accuracy, AUC and MCC show a clear improvement as well. Using the 90 most important wavelengths, a sensitivity of 0.92, specificity of 0.96, accuracy of 0.92, AUC of 0.95 and MCC of 0.88 were achieved.

Table 1. Classification results of ex-vivo colorectal cancer tissue, using DRS spectra acquired with the side-firing optical probe, in case all features were used as input and in case only the most important features were selected using MRMR analysis.

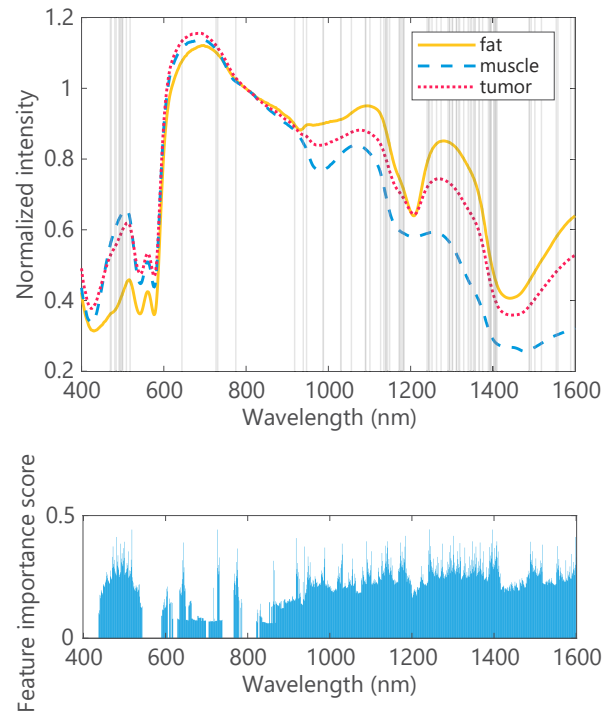|	Features	
	All	**MRMR**
	(n = 1201)	(n = 90)
Sensitivity	0.88	0.92
Specificity	0.94	0.96
Accuracy	0.88	0.92
AUC	0.94	0.95
MCC	0.82	0.88

Fig. 13. Top: Mean DRS spectra for fat, muscle and tumor tissue, acquired with the side-firing optical probe in ex-vivo colorectal cancer specimens. The grey lines highlight the 90 most important wavelengths that were selected using MRMR analysis. Bottom: Feature importance scores of MRMR analysis for every wavelength.

6.   Discussion

In this study, the feasibility of using side-firing optical fibers for DRS-based tissue discrimination during colorectal cancer surgery was assessed. The use of side-firing fibers would enable the development of more compact optical probe designs and the use of optical tissue sensing in narrow spaces that are difficult to reach with conventional optical probes using flat-tipped fibers. The novel contributions of this paper can be summarized as follows: 1) We designed a new compact optical probe with side-firing fibers, that makes it possible to perform tissue sensing measurements in narrow spaces during surgery and directly underneath your fingertip. 2) We performed Monte-Carlo simulations to explore any differences in light behaviour and measurement depth between side-firing fibers and conventional flat-tipped fibers. 3) We experimentally validated the results of Monte-Carlo simulations and the feasibility of predicting layer thicknesses in an experimental setup using a bilayer phantom. The spectra acquired with side-firing fibers were compared with flat-tipped fibers to investigate any differences in measurement depth. 4) We acquired a dataset with broadband diffuse reflectance spectra on freshly excised colorectal cancer specimens, which was correlated with histopathology results. 5) We developed a machine learning classification model to accurately discriminate tumor tissue from multiple types of healthy colorectal tissue (fat and muscle).

Monte Carlo simulations were performed to compare the light behaviour and measurement depth of side-firing fibers and conventional flat-tipped fibers. The simulations showed differences in the shape of the Jacobian profiles, between the two fiber configurations. Both the head-on profiles (Fig. 7) and side profiles (Fig. 8) showed a reduced signal using the side-firing fibers

compared to the flat-tipped fibers, at an equal source-to-detector distance. Even when comparing the relative sensitivity over distance, the side-firing fibers have a reduced measurement depth (Fig. 9). This means that care has to be taken when comparing the results from both fibers, since an equal source-detector separation distance will not necessarily measure the same volume. This discrepancy in the measurement volume might be important in multi-layer structures when comparing the results between the flat-tipped fibers and the side-firing fibers. If a specific measurement depth is an important factor in the imagined use case, a separate Monte-Carlo study might increase the understanding of the light propagation in the specific situation. Furthermore, the simulations performed in this paper were done with homogeneous tissue and generic tissue. For a specific application of side-firing fibers where the profile and measurement depth is needed, it might be worthwhile to simulate the specific fiber geometry and tissue-specific configurations. Next to differences in measurement depth, a reduction in signal can also be seen when using side-firing fibers. While this can be compensated for in several ways, it is important that care has to be taken when switching from flat-tipped fibers to side-firing fibers.

A factor that is not included in the Monte Carlo simulations, but might affect the resulting spectra, is cross-talk between the side-firing fibers. Due to the placement of the fibers, there will be light interaction between the emitting and receiving fiber that is not due to light-tissue interactions. This cross-talk between the fibers will also create a difference in the measured spectra between the two types of fiber configurations, not related to the factors described in the Monte Carlo simulations. However, the fact that other applications of side-firing fibers have shown the possibility to extract tissue-specific parameters from DRS spectra [22,23,25,26], and this paper shows the possibility to discriminate tissue types with a high accuracy using a machine learning-based approach, suggests that this effect is not too substantial to hinder the applications. Future research could investigate the effect of cross-talk between the fibers in more detail to further understand and quantify the difference between flat-tipped fibers and side-firing fibers.

As a next step, these differences in measurement depth and sensitivity have been experimentally validated using a bilayer phantom, together with the feasibility of using side-firing fibers for layer thickness prediction. The DRS spectra that were acquired on the bilayer phantom using the side-firing fibers showed a clear dip in reflectance intensity around 664 nm (peak absorption wavelength of Methylene blue in the bottom layer) for the smaller top layer thicknesses, and this dip nearly disappeared for a top layer thickness of 5 mm (Fig. 10(a)). So for this particular phantom composition, the side-firing fibers measured up to a depth of approximately 5 mm. While scattering and absorption agents were used in the phantom to mimic tissue, the conditions may not have been exactly comparable to human colorectal tissue. The maximum measurement depth of the light, when using side-firing fibers, may be different in colorectal tissue. Additionally, the measurement depth of light in tissue differs per wavelength, while the spectral analysis in this study focused on the absorption area of Methylene blue. Furthermore, a clear correlation could be seen between the top layer thickness and the reflectance intensity around 664 nm (Fig. 10(a)). In previous research, we showed that by training a regression model using broadband DRS spectra acquired with flat-tipped fibers, layer thicknesses could be predicted with an accuracy of up to 0.35 mm [34]. In the current study, using side-firing optical fibers, the top layer thickness of the bilayer phantom could be predicted with an accuracy of 0.18 ± 0.14 mm, which is comparable to the accuracy when using flat-tipped fibers. The true top layer thickness was determined by slicing the phantom at the measured locations and measuring the top layer thickness with a ruler, which might induce small inaccuracies in the ground truth. The high prediction accuracy that was found falls within the accuracy limit of 0.25 mm when reading the ruler, which demonstrates the adequacy of the DRS spectra acquired with side-firing fibers for depth prediction applications, such as margin assessment during surgery.

Figure 11 showed the DRS spectra that were acquired using conventional flat-tipped fibers, at the same locations on the phantom as using side-firing fibers. The probe configuration (SDD)

clearly influences the measured DRS spectrum, especially in the Methylene blue absorption region. In DRS, the sampling is depending on the distance between the source and detector fiber [36]. The size of the Methylene blue absorption dip increases for larger SDDs, which shows that more absorption has taken place in this wavelength range. Therefore, more light travelled through the bottom layer of the phantom and a larger sampling depth was reached. In order to assess any differences in measurement depth between side-firing fibers and flat-tipped fibers, the location-wise correlation coefficient between the DRS spectra of both fiber types is calculated for all measured locations on the phantom (Fig. 12). The results showed that the spectra of the side-firing fiber probe with an SDD of 2.7 mm were comparable with the spectra of the flat-tipped probe with an SDD of 1 to 2 mm. This indicates that an optical probe with side-firing fibers has a smaller measurement depth compared to an optical probe with flat-tipped fibers using the same source-to-detector distance, which confirms the results of the Monte Carlo simulations as shown in Section 3.1. These measurements give a relative indication of differences between the two types of fibers, with a limited number of SDDs of the flat-tipped fibers that were compared with the side-firing fibers. Additional research is necessary for an exact experimental validation of the measurement depths of both types of fibers in an absolute sense. However, the current study shows that there are differences in measurement depth between side-firing fibers and flat-tipped fibers, which is important to take into account during probe design for a specific application and comparing results from different probe configurations.

Finally, the feasibility of colorectal tissue classification using the developed compact side-firing fiber probe and diffuse reflectance spectroscopy was examined using freshly excised colorectal cancer specimens. After labelling the measured DRS spectra with the corresponding tissue types based on histopathology, the mean spectra per tissue type were calculated and shown in Fig. 13. Clear differences can be seen between tumor tissue and healthy colorectal muscle and fat tissue at several places in the spectrum. By training a quadratic SVM model the tissue types could be classified with a sensitivity of 0.88, specificity of 0.94, accuracy of 0.88, AUC of 0.94 and MCC of 0.82 when using all wavelengths as input. The relatively low number of samples compared to the number of features is one of the limitations of this study. Therefore, a MRMR feature selection algorithm was applied to select the most important wavelengths from the DRS spectra to prevent overfitting while training the classification model. Using only these most important features, the tissue discrimination performance improved to a sensitivity of 0.92, specificity of 0.96, accuracy of 0.92, AUC of 0.95 and MCC of 0.88 (Table 1). This shows that using a select number of features helped to improve the generalization of the model and achieve better results while testing. In addition, the MRMR feature importance analysis showed that the most important features were located across the entire DRS spectrum (grey lines in Fig. 13), which means that both the visible and the near-infrared part of the spectrum are important for the discrimination between tumor and healthy colorectal tissue. In previous research on colorectal tissue classification using a DRS probe with flat-tipped optical fibers, overall classification accuracy values of 0.91 [14,16], 0.94 [17], and 0.95 [15] were reported. In the current study, an overall accuracy of 0.92 was achieved, which is comparable to the previous results in the literature and suggests that tissue discrimination using a compact DRS probe with side-firing optical fibers seems feasible.

This study is the first study into the use of a compact broadband DRS probe with side-firing optical fibers for intra-operative tissue discrimination. The light behaviour and the tissue discrimination capabilities were assessed and compared to flat-tipped fibers in several steps; Monte Carlo simulations, a tissue-mimicking phantom and an ex vivo study with freshly excised colorectal specimens. The next steps would include an in vivo study to evaluate the tissue classification performance during surgery. Current research on DRS for tumor detection is focused on detecting tumor tissue close to the surface to be able to assess the circumferential resection margin (CRM). Using conventional optical probes with flat-tipped fibers it is difficult-to-reach these areas deep in the pelvis where the circumferential margin is at risk. For this

reason, clinical studies have hardly been performed yet. A compact DRS probe with side-firing fibers, on the other hand, would enable optical tissue sensing in these difficult to reach areas. Compact side-firing fiber probes might also be useful for laparoscopic/robotic surgeries. In the last decades, laparoscopic/robotic surgery has become an increasingly used alternative to open surgery. However, due to the lack of tactile feedback it is often difficult for the surgeon to determine the transection plane of the bowel distal to the tumor in low situated rectal cancers. When this transection plane is too close to the tumor the resection margin is at risk, while when the plane is too wide residual rectal volume may be too small to guarantee fecal continence. Lastly, side-firing optical fibers open up possibilities for the implementation of optical tissue sensing techniques in surgical devices, not only for colorectal cancer applications but also for other oncological and surgical fields, especially for hard to reach locations.

7. Conclusion

In this study, the feasibility of using side-firing optical fibers instead of flat-tipped optical fibers for DRS-based tissue discrimination during colorectal cancer surgery was examined. Monte Carlo simulations showed a reduced measurement depth and signal for the side-firing fibers, compared to the flat-tipped fibers. This was experimentally confirmed in a bilayer phantom study. These differences should be taken into account when using these fibers, for example by adjusting the source-to-detector fiber distance and integration times accordingly. In addition, the top layer thickness at every measured location on the phantom could be accurately predicted with a mean error of 0.18 ± 0.14 mm, which could ultimately translate to surgical resection margin assessment. In a pilot study with freshly excised colorectal cancer specimens, the spectra acquired with the side-firing fibers showed a clear difference between healthy and tumor tissue and tissue types could be discriminated with an accuracy of 0.92. These results provide opportunities for the development of smaller fiber optic probes in other applications with a small workspace as well, such as laparoscopic surgery.

References

1. H. Sung, J. Ferlay, R. L. Siegel, M. Laversanne, I. Soerjomataram, A. Jemal, and F. Bray, "Global Cancer Statistics 2020: GLOBOCAN Estimates of Incidence and Mortality Worldwide for 36 Cancers in 185 Countries," CA: A Cancer J. Clin. **71**(3), 209–249 (2021).
2. I. D. Nagtegaal and P. Quirke, "What is the role for the circumferential margin in the modern treatment of rectal cancer?" J. Clin. Oncol. **26**(2), 303–312 (2008).
3. K. F. Birbeck, C. P. Macklin, N. J. Tiffin, W. Parsons, M. F. Dixon, N. P. Mapstone, C. R. Abbott, N. Scott, P. J. Finan, D. Johnston, and P. Quirke, "Rates of circumferential resection margin involvement vary between surgeons and predict outcomes in rectal cancer surgery," Ann. Surg. **235**(4), 449–457 (2002).
4. R. Detering, M. L. Rutgers, W. A. Bemelman, R. Hompes, and P. J. Tanis, "Prognostic importance of circumferential resection margin in the era of evolving surgical and multidisciplinary treatment of rectal cancer: A systematic review and meta-analysis," Surgery **170**(2), 412–431 (2021).
5. T. E. Bernstein, B. H. Endreseth, P. Romundstad, and A. Wibe, "What is a safe distal resection margin in rectal cancer patients treated by low anterior resection without preoperative radiotherapy?" Color. Dis. **14**(2), e48–e55 (2012).
6. R. K. Orosco, V. J. Tapia, J. A. Califano, B. Clary, E. E. W. Cohen, C. Kane, S. M. Lippman, K. Messer, A. Molinolo, J. D. Murphy, J. Pang, A. Sacco, K. R. Tringale, A. Wallace, and Q. T. Nguyen, "Positive Surgical Margins in the 10 Most Common Solid Cancers," Sci. Rep. **8**(1), 5686 (2018).
7. H. S. G. Rao Tunuguntla and A. E. Gousse, "Voiding dysfunction after pelvic surgery," in *Female Urology*, Chapter 15 (Elsevier, 2008), pp. 178–186.

8. M. M. Lange and C. J. van de Velde, "Long-term anorectal and urogenital dysfunction after rectal cancer treatment," Semin. Colon Rectal Surg. **21**(2), 87–94 (2010).

9. L. Lundby and J. Duelund-Jakobsen, "Management of fecal incontinence after treatment for rectal cancer," Curr. Opin. Support. Palliat. Care **5**(1), 60–64 (2011).

10. M. D. Giglia and S. L. Stein, "Overlooked long-term complications of colorectal surgery," Clin. Colon Rectal Surg. **32**(03), 204–211 (2019).

11. W. Attaallah, C. Ertekin, I. Tinay, and C. Yegen, "High rate of sexual dysfunction following surgery for rectal cancer," Ann. Coloproctol. **30**(5), 210–215 (2014).

12. G. Zonios, L. T. Perelman, V. Backman, R. Manoharan, M. Fitzmaurice, J. Van Dam, and M. S. Feld, "Diffuse reflectance spectroscopy of human adenomatous colon polyps in vivo," Appl. Opt. **38**(31), 6628–6637 (1999).

13. Z. Ge, K. T. Schomacker, and N. S. Nishioka, "Identification of colonic dysplasia and neoplasia by diffuse reflectance spectroscopy and pattern recognition techniques," Appl. Spectrosc. **52**(6), 833–839 (1998).

14. G. C. Langhout, J. W. Spliethoff, S. J. Schmitz, A. G. Aalbers, M. L. Van Velthuysen, B. H. Hendriks, T. J. Ruers, and K. F. Kuhlmann, "Differentiation of healthy and malignant tissue in colon cancer patients using optical spectroscopy: a tool for image-guided surgery," Lasers Surg. Med. **47**(7), 559–565 (2015).

15. E. J. M. Baltussen, P. Snaebjornsson, S. G. B. de Koning, H. J. C. M. Sterenborg, A. G. J. Aalbers, N. Kok, and G. L. Beets, "Diffuse reflectance spectroscopy as a tool for real-time tissue assessment during colorectal cancer surgery," J. Biomed. Opt. **22**(10), 1–6 (2017).

16. E. J. M. Baltussen, H. J. C. M. Sterenborg, T. J. M. Ruers, and B. Dashtbozorg, "Optimizing algorithm development for tissue classification in colorectal cancer based on diffuse reflectance spectra," Biomed. Opt. Express **10**(12), 6096 (2019).

17. M. S. Nogueira, S. Maryam, M. Amissah, H. Lu, N. Lynch, S. Killeen, M. O'Riordain, and S. Andersson-Engels, "Evaluation of wavelength ranges and tissue depth probed by diffuse reflectance spectroscopy for colorectal cancer detection," Sci. Rep. **11**(1), 798 (2021).

18. E. J. Baltussen, S. G. Brouwer De Koning, J. Sanders, A. G. Aalbers, N. F. Kok, G. L. Beets, B. H. Hendriks, H. J. Sterenborg, K. F. Kuhlmann, and T. J. Ruers, "Tissue diagnosis during colorectal cancer surgery using optical sensing: an in vivo study," J. Transl. Med. **17**(1), 333 (2019).

19. G. Keiser, F. Xiong, Y. Cui, and P. P. Shum, "Review of diverse optical fibers used in biomedical research and clinical practice," J. Biomed. Opt. **19**(8), 080902 (2014).

20. U. Utzinger and R. R. Richards-Kortum, "Fiber optic probes for biomedical optical spectroscopy," J. Biomed. Opt. **8**(1), 121–147 (2003).

21. J. J. Davenport, M. Hickey, J. P. Phillips, and P. A. Kyriacou, "Method for producing angled optical fiber tips in the laboratory," Opt. Eng. **55**(2), 026120 (2016).

22. C. Lubawy and N. Ramanujam, "Endoscopically compatible near-infrared photon migration probe," Opt. Lett. **29**(17), 2022–2024 (2004).

23. B. Yu, E. S. Burnside, G. A. Sisney, J. M. Harter, C. Zhu, A.-H. Dhalla, and N. Ramanujam, "Feasibility of near-infrared diffuse optical spectroscopy on patients undergoing imageguided core-needle biopsy," Opt. Express **15**(12), 7335–7350 (2007).

24. C. Zhu, E. S. Burnside, G. A. Sisney, L. R. Salkowski, J. M. Harter, B. Yu, and N. Ramanujam, "Fluorescence spectroscopy: an adjunct diagnostic tool to image-guided core needle biopsy of the breast," IEEE Trans. Biomed. Eng. **56**(10), 2518–2528 (2009).

25. B. Yu, A. Shah, B. Wang, N. Rajaram, Q. Wang, N. Ramanujam, G. M. Palmer, and M. W. Dewhirst, "Measuring tumor cycling hypoxia and angiogenesis using a side-firing fiber optic probe," J. Biophotonics **7**(7), 552–564 (2014).

26. T. M. Baran, M. C. Fenn, and T. H. Foster, "Determination of optical properties by interstitial white light spectroscopy using a custom fiber optic probe," J. Biomed. Opt. **18**(10), 107007 (2013).

27. Y. H. Ong, A. Dimofte, M. M. Kim, J. C. Finlay, T. Sheng, S. Singhal, K. A. Cengel, A. G. Yodh, T. M. Busch, and T. C. Zhu, "Reactive oxygen species explicit dosimetry for photofrin-mediated pleural photodynamic therapy," Photochem. Photobiol. **96**(2), 340–348 (2020).

28. A. B. Karpiouk, B. Wang, and S. Y. Emelianov, "Development of a catheter for combined intravascular ultrasound and photoacoustic imaging," Rev. Sci. Instrum. **81**(1), 014901 (2010).

29. M. Basij, Y. Yan, S. S. Alshahrani, H. Helmi, T. K. Burton, J. W. Burmeister, M. M. Dominello, I. S. Winer, and M. Mehrmohammadi, "Miniaturized phased-array ultrasound and photoacoustic endoscopic imaging system," Photoacoustics **15**, 100139 (2019).

30. M. Basij, A. Karpiouk, I. Winer, S. Emelianov, and M. Mehrmohammadi, "Dual-illumination ultrasound/ photoacoustic system for cervical cancer imaging," IEEE Photonics J. **13**(1), 1–10 (2021).

31. Q. Fang and S. Yan, "Graphics processing unit-accelerated mesh-based Monte Carlo photon transport simulations," J. Biomed. Opt. **24**(11), 1 (2019).

32. A. R. Gardner, C. K. Hayakawa, and V. Venugopalan, "Coupled forward-adjoint Monte Carlo simulation of spatial-angular light fields to determine optical sensitivity in turbid media," J. Biomed. Opt. **19**(6), 065003 (2014).

33. S. L. Jacques, "Optical properties of biological tissues: A review," Phys. Med. Biol. **58**(11), R37–R61 (2013).

34. F. Geldof, B. Dashtbozorg, B. H. Hendriks, H. J. Sterenborg, and T. J. Ruers, "Layer thickness prediction and tissue classification in two-layered tissue structures using diffuse reflectance spectroscopy," Sci. Rep. **12**(1), 1698 (2022).

35. H. Peng, C. Ding, and F. Long, "Minimum redundancy, maximum relevance feature selection," IEEE Intelligent Systems **20**, 70–71 (2005).

36. R. Hennessy, W. Goth, M. Sharma, M. K. Markey, and J. W. Tunnell, "Effect of probe geometry and optical properties on the sampling depth for diffuse reflectance spectroscopy," J. Biomed. Opt. **19**(10), 107002 (2014).